Double lamellar morphologies and odd-even effects in two and three dimensional *N*,*N*′-bis(*n*-alkyl)-naphthalenediimide materials

Andreas T. Rösch, Robby Reynaerts, Brigitte A.G. Lamers, Kunal S. Mali, Steven De Feyter*, Anja R. A. Palmans, and E.W. Meijer*

ABSTRACT: The fabrication of highly ordered nanostructured surfaces is desirable in supramolecular chemistry and envisaged to bolster advances in heterogenous catalysis and microelectronic applications. Here we report on a novel set of alkylated double *N*,*N*′-bis(*n*-alkyl)-naphthalenediimides (NDIs) for the functionalization of highly oriented pyrolytic graphite (HOPG) with precise double lamellar morphologies. A detailed analysis of the two-dimensional (2D) self-assembled monolayers by scanning tunneling microscopy (STM) reveals that the structural repeating unit of the double lamellae is tuned precisely by the length of the alkyl chain that is connecting the NDI units. However, the expected odd-even effect is disturbed within the monolayers of the series of homologues. In contrast, a clear odd-even effect is observed for the melting temperatures of the respective bulk materials. Small angle X-ray scattering reveals that these bulk materials exhibit nanophase-separated lamellar phases with domain spacings that are slightly larger than the repeating units of the double lamellar structures formed on the HOPG surface. The discrepancy is assigned to a partial desorption of the alkyl spacer from the HOPG surface, which becomes more pronounced when increasing its length. Our findings suggest that this lengthening increases the conformational freedom of the molecules on surface while retaining a double lamellar morphology.

■ INTRODUCTION

The realization of highly regular patterns on surfaces has become a major goal in the fields of supramolecular chemistry and nanotechnology[1−6] since it is considered a crucial step towards achieving novel functional surfaces with applications in organic electronics,[7,8] analyte-recognition[9] and heterogenous catalysis.[10] As an attractive alternative to top-down methods that commonly involve lithographic steps,[11] bottom-up chemistries aim for the precise and highly regular positioning of molecules *via* the formation of directional, non-covalent interactions.[12−14]

The non-covalent interactions that are typically used to generate patterned surfaces are well-known from supramolecular chemistry[15] and comprise van der Waals interactions,[16−19] hydrogen-bonding,[20−26] halogen-bonding[27,28] and coordination chemistry.[29−31] In contrast to supramolecular structures that are prominent in solution or bulk systems, the morphologies formed at surfaces depend on additional parameters. When designing adsorbates rationally, adsorbate-adsorbate, adsorbate-solvent and substrate-adsorbate interactions need to be considered.[32] Achieving a suitable interplay of the interactions between all components and optimizing the preparation techniques is required for the formation of two dimensional (2D) supramolecular monolayers in high regularity.[33] A structural investigation of monolayers is often performed by atomic force microscopy (AFM)[34,35] or scanning tunneling microscopy (STM)[36] since these techniques offer a (sub)molecular resolution.[37] Typical examples for the morphologies that have been observed for self-assembled monolayers are honeycomb patterns or lamellae[38] which can exhibit structural details such as chiral textures[39] and vertical nanophase separation.[40] In addition, monolayers formed by a series of homologues may exhibit a periodical structural rearrangement that is governed by an odd-even effect.[41,42]

Odd-even effects are well-known phenomena in chemistry and physics.[41−47] One of the most prominent examples is the non-linear increase of the melting temperatures of *n*-alkanes.[48,49] The addition of one methylene group to an *n*-alkane of odd chain length is accompanied by a rather distinct increase of the melting temperature. When a methylene group is added to an *n*-alkane of even chain length, however, the melting temperature is increased only marginally or even slightly decreased.[48,49] The odd-even effect of the melting temperatures stems from differences in the crystal packing within the series of homologues. Although all compounds crystallize in the all-*anti* conformation, homologues with an even number of methylene groups form more densely packed crystals. Owing to the denser crystal packing, the homologues with an even number of methylene groups exhibit somewhat higher melting temperatures than their neighbors that contain an odd-number of methylene groups.[48,50]

On highly oriented pyrolytic graphite (HOPG) surface, adsorbed *n*-alkanes arrange in an all-*anti* conformation, since the epitaxial adsorption energy for each methylene group in a 2D monolayer is 64 meV (1.5 kcal/mol).[32] Owing to this all-*anti* conformation, the terminal methylene groups are pointing either to one side (*syn*) or to opposite sides (*anti*) of the molecule. As a result, supramolecular monolayers prepared from alkyl chain functionalized molecules typically exhibit a periodic modulation of surface structures that follows an odd-even trend.[41] An exemplary STM study describing such an odd-even effect on HOPG surface has

been conducted by Kim *et al.*[51] They investigated the adsorption of dicarbamates that were both connected and terminated by alkyl chains on HOPG surface. Given by the all-*anti* conformation of the adsorbed alkyl chains, an even number of methylene groups in the central alkyl chain resulted in an *anti*-arrangement of the terminal alkyl chains with respect to each other. Analogously, a *syn*-arrangement was observed for derivatives containing an odd number of methylene groups in the central alkyl chain. Since AFM and STM only image the surface morphologies, other techniques such as nuclear magnetic resonance (NMR),[52] differential scanning calorimetry (DSC),[52] attenuated total internal reflection infrared spectroscopy (ATR-IR),[53] electron diffraction,[54] neutron[52,53,55,56] and X-ray scattering[56–58] become more suitable to obtain structural information once multilayered or bulk materials are formed. Previous studies indicate that the structure of the physisorbed self-assembled monolayer does not necessarily represent a 2D slice of the 3D crystal of the same material. This is due to the additional interactions prevalent at the solution-solid interface.[59,60]

The ability of *N*,*N'*-bis(*n*-alkyl)naphthalenediimides (NDIs) to form self-assembled structures in crystalline bulk material[58,61–64] and on surface[14,38,40,59,65] has been studied in detail. This class of compounds is of particular interest due to n-type semiconducting properties[62,66–69] and straightforward chemical modification.[62,63,70] The determination of the crystal structures of various alkylated NDIs indicated that in bulk, the compounds are typically arranged in lamellar phases.[58] The domain spacings of the investigated crystals were defined by the molecular dimensions of the microphase segregated NDI cores and the alkyl chains of the molecules.[58] In contrast to bulk materials, the self-assembled monolayers formed on HOPG surfaces showed the formation of lamellar structures only for very short or rather long alkyl chains ($N_{\text{methylene groups}} \leq 4$ or ≥ 13). For the derivatives that contained alkyl chains of intermediate length ($4 < N_{\text{methylene groups}} < 13$), the formed morphologies were identified as honeycomb patterns. The hexagonal packing of the NDI cores in these honeycomb patterns was ascribed to a partial desorption of the alkyl chains.[38]

Inspired by a recent report on engineering long-range order in supramolecular assemblies of alkylated NDIs,[14] here we report on the design of novel double NDIs (Scheme 1) to probe the impact of a covalent connection between two NDI cores on the self-assembly behavior. We terminated the double NDIs with octadecyl chains to induce the formation of lamellar morphologies on HOPG surface.[14,38] The length of the alkyl spacer was varied from three to twelve carbon atoms to systematically investigate structure-property relationships of both self-assembled monolayers and bulk phases. STM was used to characterize the structure of the self-assembled monolayers in 2D whereas X-ray scattering was employed to investigate the morphologies and corresponding domain spacing in the bulk phase.

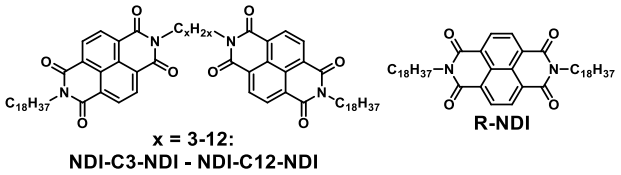

Scheme 1. Molecular structures of double *N,N'*-bis(*n*-alkyl)-naphthalenediimides **NDI-C3-NDI** – **NDI-C12-NDI** and the reference **R-NDI**.

■ EXPERIMENTAL SECTION

STM measurements: STM samples were prepared under ambient conditions by applying a drop of the saturated solution of a given double NDI derivative onto a freshly cleaved HOPG surface (HOPG, grade ZYB, Advanced Ceramics Inc., Cleveland, OH) followed by creating a solution flow by touching one corner of the HOPG sample with a clean Kimwipe tissue paper after which the sample was heated at 100°C for 10 minutes. This annealing step led to evaporation of the solvent. Hence a drop of neat solvent was applied to the surface prior to imaging. The STM experiments were carried out using a PicoSPM (Agilent) operating in the constant-current mode with the tip immersed in the solution at room temperature. STM tips were prepared by mechanical cutting from Pt/Ir wire (80%/ 20%, diameter 0.2 mm). For analysis purposes, the imaging of a molecular layer was immediately followed by recording at a lower bias voltage the graphite lattice, under otherwise identical experimental conditions. The STM images were corrected for drift via Scanning Probe Image Processor (SPIP) software (Image Metrology ApS), using the recorded graphite images for calibration purposes, allowing a more accurate unit cell determination. The unit cell parameters were determined by examining at least 5 images and only the average values are reported. After the determination of the unit cell from the acquired STM images, a molecular model of the observed monolayer was constructed using HyperChem™ Professional 8.0.1 program. First, a molecular model for a single molecule was built. The model of the entire monolayer was constructed by placing the molecules in accordance with the unit cell parameters obtained from the analysis of the calibrated STM images. The imaging parameters are indicated in the figure caption: tunneling current (I_{set}), and sample bias (V_{bias}).

Characterization of the thermal properties: POM was performed on an optical microscope from Jenaval. Images were recorded using an Infinity1 camera provided by Lumenera. Samples for polarized optical microscopy (POM) imaging were drop casted on glass coverslips, heated above the isotropic melt and slowly cooled (10 °C/min). The POM study was started by isotropically melting the samples. The POM images were taken while the sample was cooled from the isotropic melt to room temperature and heated again to the isotropic melt. DSC was performed on a Q2000 from TA Instruments. For the DSC measurements, all samples were heated to the isotropic melt, equilibrated, and cooled down at a constant rate of 10 K min^{-1} to standardize the thermal history. Subsequently, two heating and cooling cycles were recorded by DSC.

X-Ray scattering: Bulk small angle X-ray scattering (SAXS) was performed on an instrument from Ganesha Lab. The flight tube and sample holder are all under vacuum in a single housing, with a GeniX-Cu ultralow divergence X-ray generator. The source produces X-rays with a wavelength (λ) of 0.154 nm and a flux of 1 × 108 ph s-1. Scattered X-rays were captured on a 2D Pilatus 300K detector with 487 × 619 pixel resolution. The sample-to-detector distance was 0.084 m (WAXS mode) or 0.48 m (MAXS mode). The instrument was calibrated with diffraction patterns from silver behenate. To determine the bulk morphologies and corresponding domain spacings, the packing of the NDI bulk materials was investigated by X-ray scattering. The samples were prepared by placing the NDIs in SAXS capillaries, heating them to the isotropic melt and cooling down slowly. Subsequently, 2D transmission scattering data were acquired in medium- and wide-angle modes (MAXS and WAXS, $0.1 < q < 30$ nm^{-1}). Radial averaging resulted in one-dimensional (1D) transmission scattering profiles that captured feature sizes in a range of 0.2 – 60 nm.

■ RESULTS AND DISCUSSION

Synthesis. The synthesis of all NDIs was performed according to Scheme 2. Following a modified protocol by Tambara *et al.*,[71] *n*-octadecylamine **1** was reacted with 1,4,5,8-naphthalenetetracarboxylic dianhydride **2**. The condensation was sped up by using a microwave reactor. Compound **2** was used in excess to form predominantly octadecyl naphthalene monoimide **NMI** and reduce the formation of double alkyl functionalized **R-NDI**. During the work-up, unreacted **2** was solubilized in water by hydrolysis in aqueous NaOH solution (c = 1 M). Insoluble **NMI** was isolated by filtration and dispersed in aqueous hydrochloric acid solution (3 M) to protonate the carboxylic acid groups. The protonation was required to increase the electrophilicity of the compound for the subsequent condensation reaction. Dried **NMI** was reacted with aliphatic α,ω-diamines (ranging from 1,3-diaminopropane to 1,12-diaminododecane) using the microwave reactor. All double NDIs **NDI-C3-NDI** – **NDI-C12-NDI** were purified by recrystallization from chloroform or toluene and obtained as crystalline compounds in medium to high yields (34-81%). In addition to the double NDIs, 1,4,5,8-naphthalenetetracarboxylic dianhydride was also reacted twice with *n*-octadecylamine to prepare the reference compound **R-NDI**. After recrystallization from toluene, **R-NDI** was obtained as a crystalline material in high yield (86%).

The compounds were fully characterized by ^{1}H and ^{13}C nuclear magnetic resonance (NMR) spectroscopy, matrix-assisted laser ionization time of flight mass spectrometry (MALDI-TOF-MS) and Fourier-transform infrared (FT-IR) spectroscopy. The individual spectra are depicted in the ESI. The results show that the final compounds were obtained in high purity. For all compounds, absorbance and fluorescence spectra were determined in solution and solid state. See the ESI for individual spectra (Figures S1-S24) and a supplementary discussion on the optical properties.

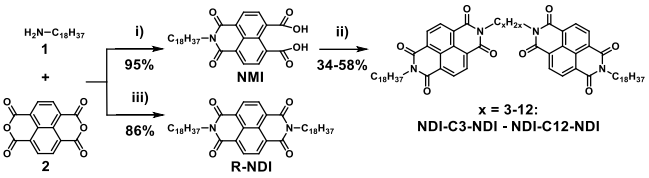

Scheme 2. Synthetic route for the preparation of double NDIs **NDI-C3-NDI** - **NDI-C12-NDI** and **R-NDI**. Reagents and conditions: i) 1) 2.5 eq naphthalenetetracarboxylic dianhydride, 50/50 DMF/THF, 75 °C - 140 °C, 10 min, 2) $NaOH_{(aq.)}$, 3) $HCl_{(aq.)}$, ii) aliphatic α,ω-diamines, DMF/THF, 75 °C - 140 °C, 30 min, iii) 2 eq. *n*-octadecylamine, DMF/THF, 75 °C - 140 °C, 10 min.

Physisorbed Self-Assembled Monolayers formed at the Solution/HOPG Interface. Given the low solubility of the double NDIs in 1-phenyloctane (boiling point of 261-263 °C), a typical solvent used for STM experiments, the self-assembled monolayers were obtained by drop casting saturated solutions onto freshly cleaved HOPG substrates. Drop-casting was followed immediately by creating a solution flow by absorbing the excess solution using a clean tissue paper since flow-deposition is a known procedure to increase the domain size of physisorbed self-assembled monolayers.[33] Flow-deposition was followed by annealing the samples at 100° C for 10 minutes. The HOPG substrates were allowed to slowly cool down to room temperature before the STM measurements were performed.

Using these conditions to prepare the samples, the monolayers formed by all double NDIs (except for **NDI-C4-NDI** whose solubility was too low) could be imaged. Submolecular resolution STM images of the monolayers are provided in Figure 1. Corresponding unit cell parameters are given in Table 1. The images indicate the formation of double lamellar structures for all compounds. In general, the double lamellar structures consist of alternating bright and dark columns. The bright columns always have a similar width and are separated by a narrower dark column on the one side (grey arrows in Figure 1) and a wider dark column on the other (green arrows in Figure 1). Within the series of compounds, the STM images clearly reveal a variation of the width of the narrower dark column that was assigned to the adsorption of the alkyl spacer connecting the two NDI cores. The broader dark columns were attributed to the terminal octadecyl chains and the bright columns to the adsorbed NDI cores.

The structure of the self-assembled monolayer can be better understood from the corresponding molecular models displayed in Figure 1. Figure 1a and b show the STM image of the monolayer and corresponding molecular model of **NDI-C3-NDI**. The latter was built based on the unit cell parameters of the self-assembled network obtained from calibrated STM data. Both images show two different modes of adsorption and the front at which these two regimes meet. In the so-called 'collinear' conformation (marked in red in

Figure 1b), the terminal octadecyl chains are collinear with respect to each other. Adsorption of the molecules in this conformation is associated with the formation of lamellae in which the terminal octadecyl chains are interdigitated with those from the molecules adsorbed in the adjacent lamella. In the 'non-collinear' adsorption conformation (marked in blue in Figure 1b), the terminal chains are non-collinear with respect to each other. This conformation is associated with the lamellae in which the octadecyl chains are not interdigitated. STM images provided in the supporting information not only reveal the simultaneous presence of the two types of conformations but also reveal a time-dependent transition from an interdigitated to non-interdigitated state (see Fig. S28 in the supporting information). Additionally, the two covalently connected NDI cores of **NDI-C3-NDI** are always in a *syn*-arrangement with respect to each other. Similar to **NDI-C3-NDI**, **NDI-C5-NDI** showed the adsorption into double lamellar structures in which collinear and non-collinear regimes coexisted. The two covalently connected NDI cores were arranged in the *syn*-conformation, too. In contrast, all remaining double NDIs (**NDI-C6-NDI** – **NDI-C12-NDI**) strongly preferred the adsorption in the non-collinear conformation. We note that identifying collinear and non-collinear conformation of the side chain is not restricted to realizing a specific contrast in the STM measurement as noticed by comparing Figure 1i and Figure S28. The STM images of the monolayers formed by these homologues indicated that the covalently connected NDI cores were always adsorbed in the *anti*-arrangement. The common structural element that distinguishes the non-collinear regime from the collinear regime in the monolayers of our double NDIs, is the sharp bend (between 30° to 60°) that is observed in the terminal octadecyl chains. Irrespective of whether the alkyl chains are adsorbed in interdigitated or non-interdigitated fashion, the width of the column remains virtually the same as confirmed by building alternative molecular models. We also note that despite the bend in the alkyl chains clearly visible in the STM images, the terminal octadecyloxy chains were always found to be adsorbed along one of the main symmetry axes of graphite lattice. This is readily evident upon comparison of the graphite symmetry axes provided on top of STM images against the orientation of alkyl chains visible from the STM data/molecular models that replicate the observed symmetry. This preferred alignment seems to be the driving force for self-assembly and potentially explains why no other conformation was observed. While alkyl chains are flexible and thus can form curved structures upon surface adsorption, the sharp bend indicates the formation of a kink that involves the partial desorption of the otherwise straight alkyl chain from the surface.[72] The molecular models presented above enforce this kink by introducing a gauche defect between the C2 and the C3 carbons of the terminal octadecyl chains. The coinciding presence of two modes of adsorption of the alkyl sidechains has also been reported for self-assembled monolayers of single NDIs and has been ascribed to the very similar potential energies of the two states.[14,38] Similar sharp angles as observed for our double NDIs have also been reported for the on-surface self-assembly of a hexadecyl substituted single NDI.[59] Based on DFT calculations, it was argued that the partial desorption of the methylene group in the kinked conformation avoids the steric repulsion between the carbonyl group of the NDI core and the α-CH_2 group of the alkyl chain. In addition, the bent conformation was also found to increase the overall density of the lamellar structures which added an energetically favorable contribution to the overall adsorption energy of the monolayer (illustrated schematically in Figure S25).[59]

Observing the *syn*- and *anti*-arrangement of the covalently connected NDI core is somewhat similar to the work by Kim *et al*.[51] The literature report described the adsorption of dicarbamates on HOPG surface which were both connected and terminated by alkyl chains. Depending on the number of the methylene groups in the central alkyl chain that was absorbed flat and in all-*anti* conformation to the HOPG surface, either a *syn*- or an *anti*-arrangement of the carbamates and the terminal side chains was observed. The *syn*-arrangement was observed for the compounds that contained alkyl spacers with an odd number of methylene groups. Analogously, the *anti*-arrangement was observed for compounds containing alkyl spacers with an even number of methylene groups. Since **NDI-C3-NDI** and **NDI-C5-NDI** contained alkyl spacers with an odd parity, the observed *syn*-arrangement of the NDI cores in the monolayers satisfied our expectations. Analogously, the *anti*-arrangement for **NDI-C6-NDI**, **NDI-C8-NDI**, **NDI-C10-NDI** and **NDI-C12-NDI** fulfilled the rational, too. In contrast, observing the *anti*-arrangement for the monolayers of **NDI-C7-NDI**, **NDI-C9-NDI** and **NDI-C11-NDI** was somewhat surprising. The suspension of the odd-even effect suggested that for these homologues, the central alkyl chain was not adsorbed flat in the all-*anti* conformation.

In order to understand the structural origin of the observation better, we compared the unit cell parameters '*b*' of the monolayers formed by **NDI-C7-NDI** – **NDI-C11-NDI** which corresponds to the structural repeating unit perpendicular to the lamellae. As noticed in Table 1, '*b*' was either not increased or even slightly decreased upon the transition from a homologue with an even parity to the following homologue with an odd parity. In contrast, the addition of one methylene group to a homologue with an odd parity resulted in a notable increase of '*b*'. The peculiar odd-even trend corroborated the partial desorption of the alkyl spacers with an odd number of methylene groups. As noticed in Figure 1h, l and p, we simply pointed the central methylene group of the alkyl spacer away from the surface while keeping the rest in the same plane to fit the observed structure with the molecular models. Possible reasons for the suspension of the odd-even effect are the systems' striving to the highest packing density, a higher entropy by the partial desorption of the alkyl spacer and a better interaction of the monolayer with the HOPG surface when both NDI cores were arranged in the *anti*-conformation along one axis of the underlying HOPG surface.

Table 1. Unit cell parameters of the lamellar domains formed by **NDI-C3-NDI – NDI-C12-NDI** at the 1-phenyloctane/HOPG interface.

	Unit cell parameters (STM)			rel. orientation of
Entry	*a* [nm]	*b* nm]	α [°]	the NDI cores
NDI-C3-NDI	0.9 ± 0.1	4.4 ± 0.1	87 ± 2	syn
NDI-C5-NDI	0.9 ± 0.1	4.4 ± 0.1	87 ± 2	syn
NDI-C6-NDI	0.9 ± 0.1	4.4 ± 0.1	88 ± 1	anti
NDI-C7-NDI	0.9 ± 0.1	4.4 ± 0.1	89 ± 1	anti
NDI-C8-NDI	0.9 ± 0.1	4.6 ± 0.2	89 ± 2	anti
NDI-C9-NDI	0.9 ± 0.1	4.5 ± 0.1	89 ± 1	anti
NDI-C10-NDI	0.9 ± 0.1	4.8 ± 0.1	86 ± 4	anti
NDI-C11-NDI	0.9 ± 0.1	4.7 ± 0.1	87 ± 2	anti
NDI-C12-NDI	0.9 ± 0.1	4.8 ± 0.1	85 ± 1	anti

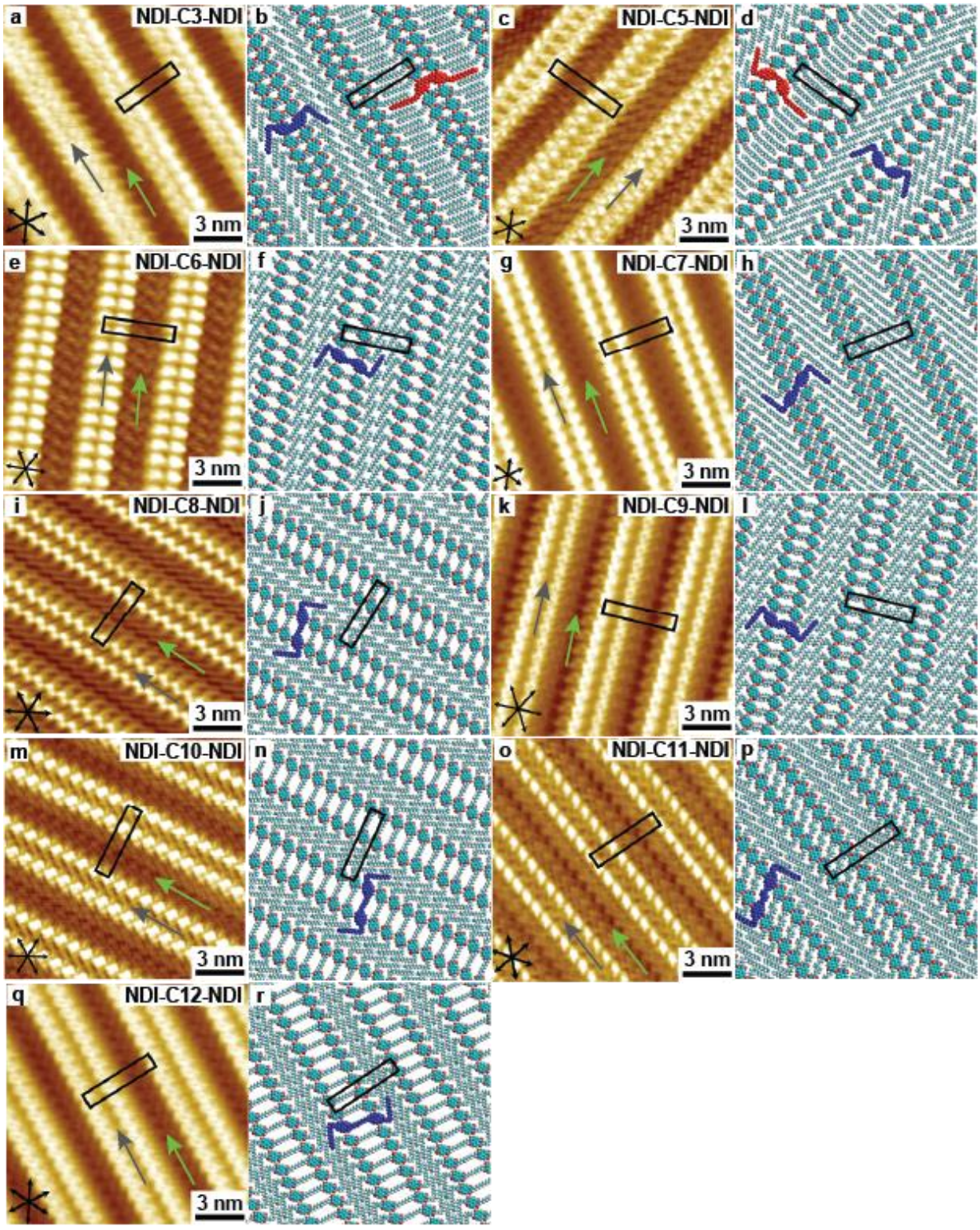

Figure 1. Representative high-resolution STM images (a, c, e, g, i, k, m, o, q) and corresponding molecular models (b, d, f, h, j, l, n, p, r) of the monolayers formed by the double NDIs at the 1-phenyloctane/HOPG interface. Imaging parameters: (a) V_{bias} = -1.0 V, I_{set} = 90 pA; (c) V_{bias} = -1.1 V, I_{set} = 110 pA; (e) V_{bias} = -0.5 V, I_{set} = 120 pA; (g) V_{bias} = -0.6 V, I_{set} = 100 pA; (i) V_{bias} = -0.6 V, I_{set} = 130 pA; (k) V_{bias} = 0.8 V, I_{set} = 110 pA; (m) V_{bias} = 0.5 V, I_{set} = 110 pA; (o) V_{bias} = -0.7 V, I_{set} =130 pA; (p) V_{bias} = -1.35 V, I_{set} = 80 pA. The orientation of the HOPG axes and the unit cell are given in black.

Large scale STM images showed that the columns in adjacent domains are oriented at an angle of approximately 60° with respect to each other (see Figure S27 in the ESI). This relative arrangement highlighted the influence of the underlying graphite substrate lattice on the self-assembly process. When samples were solely prepared by drop-casting (without the annealing and flow deposition steps), the formation of disordered aggregates was observed. After annealing, ordered domains that typically spanned 120 nm to 300 nm were obtained. Applying flow deposition[33] resulted in the preparation of the largest domains. In some cases, we observed the formation of domains that exceeded the surface area of 1 μm² (Figure S29) which suggested that the molecular design was excellent for the fabrication of supramolecular structures with long range order.

Thermal Properties. Having characterized the structural details of the surface morphologies, we continued our study with the investigation of the bulk properties. The thermal behavior of all compounds was investigated in detail by differential scanning calorimetry (DSC) and polarized optical microscopy (POM). The data obtained from the second heating cycle (heating rate of 10 K/min) are summarized in Table 2. All DSC traces are depicted in Figure S32-42. Being exemplary for the series, the DSC trace of **NDI-C11-NDI** is depicted in Figure 2. Upon heating from room temperature, two thermal transitions were noticed. The first transition, whose maximum heat flow is indicated by T_1, was only weakly endothermic and occurred over a broad temperature window that ranged from 90 °C to 150 °C. POM images which were taken below and above T_1 showed the presence of similar birefringent textures. Interestingly, fissures appeared when cooling the material below T_1 and disappeared when heating above T_1. A second thermal transition was noticed when the temperature was increased to 230 °C. At this temperature, the solid material melted into an isotropic liquid, as evidenced by the loss of the birefringence in the POM image. The corresponding thermal phase transition temperature was assigned to the melting temperature T_m.

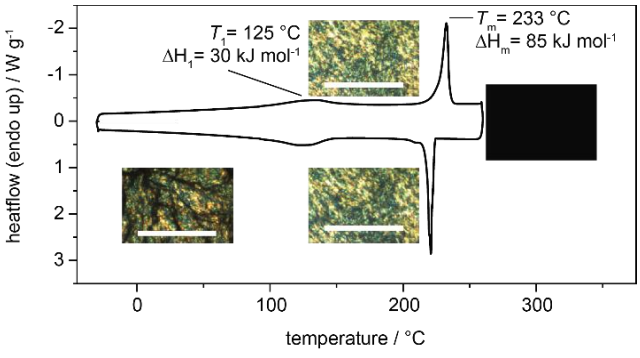

Figure 2. Second heating and cooling runs recorded by DSC for **NDI-C11-NDI** (heating and cooling rate = 10 K min^{-1}). The insets are POM images. The images were taken for the isotropic melt, after crystallization, when cooled down to 50 °C and after reheating closely beneath T_m. White scale bar: 100 μm.

The remaining homologues showed a very similar thermal phase behavior which consisted of two thermal transitions during the heating cycle (except for **NDI-C8-NDI** that showed an additional third thermal transition at T_2 = 229 °C; ΔH_2 = 7 kJ mol^{-1}) and two thermal transitions during the cooling cycle. Since the first thermal transitions of all homologues occurred over a similar and rather wide temperature range, it was not possible to detect an odd-even effect for T_1. In contrast, the melting temperatures T_m of the series of homologues depended strongly on the length of the alkyl spacer. As noticed in Figure 3a, T_m of the double NDIs was governed by an odd-even effect. Double NDIs with an even parity of the alkyl spacer always had higher melting temperatures T_m than their neighbors with an odd parity. Within the series, **NDI-C4-NDI** showed the highest (T_m = 328 °C) and **NDI-C11-NDI** (T_m = 230 °C) the lowest T_m. This observation suggested that T_m was overall decreased when the length of the alkyl spacer was increased. For the melting enthalpies ΔH_m, an odd-even effect was noticed, too (Figure 3b). In contrast to the odd-even effect of T_m, the odd-even effect of ΔH_m was not noticed through-out the entire series. **NDI-C8-NDI**, the only homologue that contained a third thermal transition, was an exception from the trend.

Since the POM images taken below and above T_1 always showed birefringent structures and the samples remained non-shearable until heated to T_m, the transitions occurring at T_1 were suggesting crystal-crystal transitions. Interestingly, the birefringent structures noticed in the POM images above and below T_1 looked very similar and were distinguished only by the formation of fissures when the sample was cooled below T_1. The observation of similar fissures during cooling perylene bisimides has been reported by Chesterfield *et al.*[73] In this system, the formation of fissures was ascribed to differences in the thermal expansion coefficients of the organic material and the microscope glass slide and could be avoided completely by reducing the cooling rate to 1 K/min. In case of our double NDIs, fissure formation was still observed at the cooling rate of 1 K/min.

A recent report on the thermal phase transitions of alkylated single NDIs showed that within the series of homologues, T_m was decreased when the length of the side chains was increased.[64] The somewhat unexpected trend of decreasing T_m while increasing the molecular weight was ascribed to an increasing fusion entropy that stemmed either from the larger conformational freedom of the longer alkyl chains in the melt or from their more ordered crystal packing in the solid.[64] The structural similarity of our double NDIs with the reported single NDIs suggested that the increase of the length of the alkyl spacer resulted in increasing the fusion entropy of the double NDIs, too. In line with this argumentation, **R-NDI**, which contains exclusively long alkyl chains, was found to reach the isotropic melt already at 147 °C which was also in accordance with the findings of Ichikawa et al.[74] The similarity of the DSC traces recorded for the series of the double NDIs was somewhat surprising

since the above-mentioned literature report on the single NDIs described the presence of multiple polymorphic transitions and liquid crystalline phases for several homologues within the series.[64] We conclude that while the length of alkyl spacer in the double NDIs induced strong differences in T_m within the series, its size was too small to counter the structural directing effect of the terminal octadecyl sidechains which induced the formation of lamellar structures for all homologues.

Since the odd-even effect that was observed for T_m stemmed from periodic changes in the crystal packing,[64] and the similarity of the DSC traces indicated no polymorphism for the double NDIs, we continued our study with a structural investigation of the bulk morphologies at room temperature and the rearrangements occurring at T_1 by performing X-ray scattering.

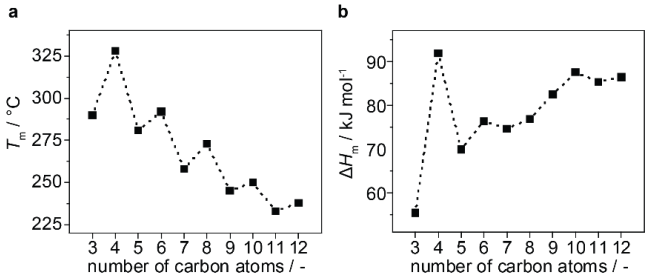

Figure 3. Decrease of the melting temperature T_m in an odd-even fashion when increasing the length of the alkyl chain connecting two octadecyl terminated NDI motifs (a). Enthalpy of melting as a function of length (b).

Supramolecular Ordering of the NDIs in Bulk Material. To determine the bulk morphologies and corresponding domain spacings, the packing of the NDI bulk materials was investigated by X-ray scattering. Since we were not able to grow single crystals of our compounds, we could not determine the crystal structure by single crystal X-ray crystallography and performed the X-ray scattering study on polycrystalline samples instead. The scattering profiles of all double NDIs are depicted in Figure 4, with the **R-NDI** as a reference. All NDIs exhibited well-structured, lamellar lattices, as indicated by the sharp, equally spaced scattering peaks in the MAXS region (labelled with q^*, $\sqrt{4}q^*$, $\sqrt{9}q^*$, ...). For **NDI-C6-NDI** and **NDI-C8-NDI**, the presence of a second lamellar lattice was noticed. For these two compounds, the sets of scattering peaks were labelled as q^* and q_2^*, respectively. Both sets of reflections remained unaltered after heating the samples again and annealing for several minutes before cooling slowly to room temperature. The lamellar spacings d_{LAM} of all crystal lattices are listed in Table 2. The graph in Figure 5 shows the variation of d_{LAM} with an increasing length of the alkyl spacer. With **NDI-C8-NDI** being an exception, d_{LAM} was found to increase with increasing length of the alkyl spacer. Additionally, the increase of d_{LAM} followed an odd-even trend. Until reaching **NDI-C8-NDI**, d_{LAM} was increased noticeably upon the transition from a homologue with an odd number of methylene groups in the alkyl spacer to a homologue with an even parity. In contrast, the transition from a homologue with an even number of methylene groups in the alkyl spacer to a homologue with an odd parity resulted only in a small increase of d_{LAM}. The odd-even effect of d_{LAM} was less apparent for the homologues that succeeded **NDI-C8-NDI**.

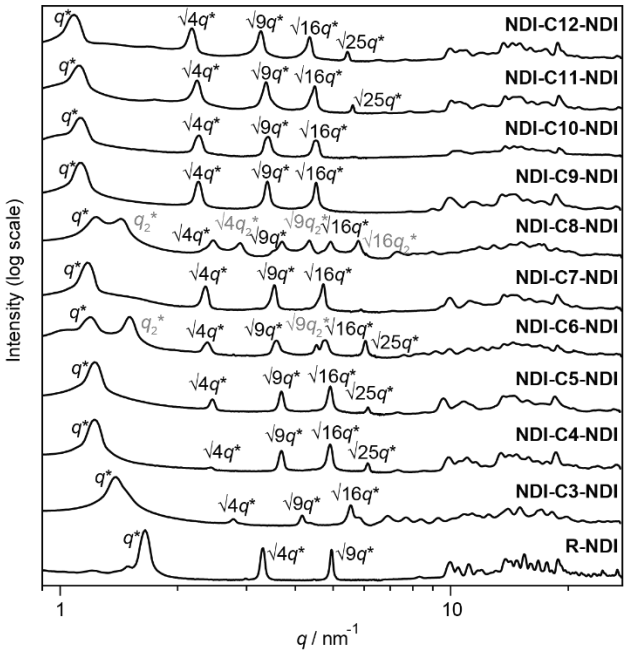

Figure 4. 1D transmission scattering profiles obtained for the double NDIs at room temperature.

The scattering peaks at 18.5 – 18.7 nm^{-1} were indicative of the crystallization of the alkyl chains in the all-*anti* conformation.[75] The combination of the lamellar morphology and the observed crystalline alkyl chain domains suggested the formation of microphase-segregated 2D sheets that contained alternating crystalline NDI and alkyl lamellae. This type of microphase-segregation has also been described for alkylated single NDIs and was assigned to the formation of van der Waals interactions between the alkyl chains and the aggregation of the NDI cores.[14,38,58,76]

To further probe for the suggested formation of the microphase- segregated NDI and alkyl sheets, we used simple modelling based on molecular mechanics to estimate the lengths of the NDI-C_xH_{2x}-NDI-$C_{18}H_{37}$-elements in the fully stretched conformation. The comparison of the calculated values with the experimentally determined d_{LAM} (Table 2) shows that d_{LAM} of the first set of reflexes was always very similar but slightly larger than the length of the NDI-C_xH_{2x}-NDI-$C_{18}H_{37}$-element. Considering that in the crystal, the octadecyl chains were only interdigitated and not covalently linking two NDI cores, the somewhat larger size of the experimentally determined d_{LAM} is in agreement with the

proposed arrangement of the double NDIs in the fully stretched conformation (illustrated schematically in Figure 6a). The second set of reflexes found for **NDI-C6-NDI** and **NDI-C8-NDI** was indicative of the formation of a second lamellar lattice stemming from a second crystalline polymorph which interestingly had not been noticed in the DSC traces. When comparing the dimensions of the two lamellar lattices for each derivative, we noticed that d_{LAM} of the second lattice was approximately 1 nm (1.1 nm for **NDI-C6-NDI** and 0.7 nm for **NDI-C8-NDI**) smaller than d_{LAM} of the first lattice. One possible arrangement that can explain the reduced d_{LAM} and still contains fully stretched terminal alkyl chains was achieved by the backfolding of the second NDI core on the first. The proposed structure of this second crystal polymorph is shown schematically in Figure 6b.

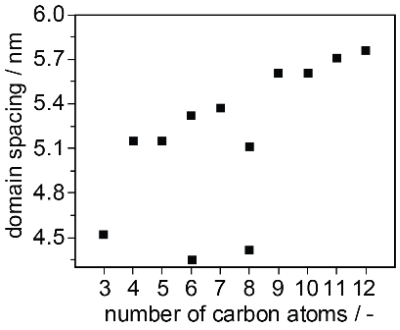

Figure 5. Lamellar domain spacing d_{LAM} of double NDIs obtained from X-ray scattering as a function of the number of carbon atoms in the alkyl chain connecting the two NDI motifs. For **NDI-C6-NDI** and **NDI-C8-NDI**, two lamellar structures with different lamellar thickness are observed.

Subsequently, variable-temperature (VT) X-ray measurements were performed to capture structural transformations that related to the transition observed at T_1 in the DSC traces. **NDI-C11-NDI** was chosen for this type of experiment since it had the lowest melting temperature T_m. A selection of 1D transmission scattering profiles recorded at variable temperatures is depicted in Figure S43. When the temperature of the heating element was increased to 260 °C, **NDI-C11-NDI**'s temperature was well above T_1 but still below T_m. In this regime we observed an increase of d_{LAM} from 5.7 nm to 6.0 nm. Furthermore, the scattering peaks in the wide-angle region (q > 8 nm^{-1}) changed. A third lamellar lattice appeared next to the second lamellar lattice when the heating element that contained the sample was heated to 270 °C. The reflexes of the lattice are labelled by q_3* and its integer multiples ($\sqrt{4}q_3$*, $\sqrt{9}q_3$*...). The corresponding d_{LAM} was increased further to 7.0 nm. At 280 °C, only this third lamellar structure remained. Heating and annealing the sample for a longer period at this temperature induced melting which was accompanied by the disappearing of the scattering peaks in the WAXS region.

Changes of the scattering peaks in the wide-angle region (q > 8 nm^{-1}) during heating indicated a transition in the local crystal packing. The successive widening of the lamellar lattice of **NDI-C11-NDI** upon heating was most likely stemming from the aliphatic side chains becoming somewhat mobile. The thermal behavior was in contrast to the thermal rearrangements reported for several alkylated single NDIs where heating was found to induce the formation of more complex crystal structures.[64] The observed widening of the lamellar lattice was also corroborating the proposed microphase-segregated sheetlike structure. Initially, heating only weakened the cohesion of the octadecyl chain sheets. Strongly aggregated NDI cores retained the 2D sheet morphology and were melted only at higher temperatures.

Table 2. Thermal properties and scattering data of the double NDIs **NDI-C3-NDI** – **NDI-C12-NDI** as well as **R-NDI**.

entry	NDI[a]	T_1[b] [°C]	ΔH_1[c] [kJ mol^{-1}]	T_m[b] [°C]	ΔH_m[c] [kJ mol^{-1}]	d_{LAM} X-Ray[f] [nm]	d_{LAM} calc.[h] [nm]
1	**NDI-C3-NDI**	96	40.9	290	55.4	4.5	4.2
2	**NDI-C4-NDI**	133	37.8	328	91.9	5.2	4.4
3	**NDI-C5-NDI**	121	41.1	281	69.9	5.2	4.5
4	**NDI-C6-NDI**	124	50.3	292	76.4	5.3 (4.2)[g]	4.6
5	**NDI-C7-NDI**	130	45.1	258	74.6	5.4	4.7
6	**NDI-C8-NDI**[e]	128	37.9	273	76.9	5.1 (4.4)[g]	4.8
7	**NDI-C9-NDI**	124	34.8	245	82.5	5.6	5.0
8	**NDI-C10-NDI**	132	27.4	250	87.5	5.6	5.1
9	**NDI-C11-NDI**	125	30.3	233	85.3	5.7	5.2
10	**NDI-C12-NDI**	132	37.4	239	86.4	5.8	5.4
11	**R-NDI**[d]	139	15.0	147	47.4	3.8	3.2

[a] Molecules as depicted in Scheme 1; [b] Tabularized temperatures for the first endothermic transition (T_1) and second endothermic transition (T_m) are the local maxima in heat flow during the second heating cycle in the DSC trace using a heating rate of 10 K min^{-1}. [c] corresponding enthalpy of fusion per mole molecule (ΔH_1 and ΔH_m, respectively). [d] **R-NDI** melts at T_1 and forms a liquid crystalline phase. For this compound, T_m represents the clearing temperature. [e] **NDI-C8-NDI** showed an addition transition at T_2 = 229 °C, ΔH_2 = 7 kJ mol^{-1}; [f] Lamellar domain spacing of the bulk phase examined with MAXS at room temperature and calculated from $d = 2\pi/q^*$; [g] A second double lamellar domain spacing was observed. The smaller spacing, which is corresponding to q_2^* (Figure 4), is reported in brackets. [h] theoretical domain spacings based on the lengths of the NDI-C_xH_{2x}-NDI-$C_{18}H_{37}$-elements constructed by molecular modelling (Figure S26).

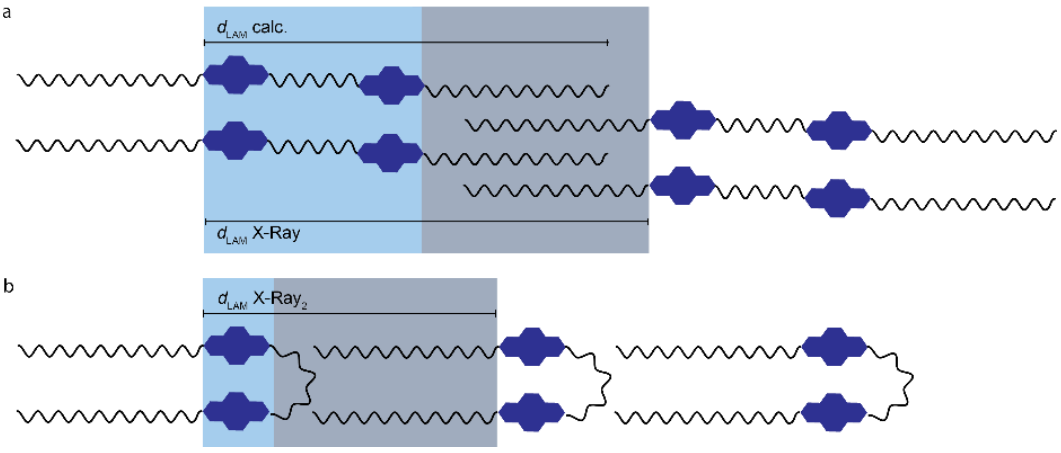

Figure 6. (a) Pictorial representations of the molecular packing of NDIs in bulk as a fully stretched and (b) backfolded arrangement.

Although we observed the formation of lamellar phases both on surface and in bulk material, a direct comparison between the structures formed in both media is not straightforward due to the differences in the interactions between the molecules in the two environments (solid state versus liquid-solid interface).[38] The two main differences between the two media are the confined nature of the 2D self-assembly process and the presence of the solid substrate and solvent molecules at the solution-solid interface. These two factors are absent in the bulk crystallization scenario. The 'structure directing' effect of the graphite lattice on self-assembled monolayers of alkylated systems is well-documented[32,77] and was also noticed in the present case. In the conformations that were observed in the self-assembled monolayers, the terminal alkyl chains and possibly also the long alkyl spacers (although not observed clearly in STM images) are always oriented along one of the symmetry axes of the underlying HOPG substrate. Such 'structure directing' influence of the substrate is absent in the case of the bulk crystalline phase. The non-collinear adsorption regime observed in monolayers indicated that the molecule-substrate interaction at the level of the single molecule was a dominant factor in the stabilization of the monolayer. Intermolecular interactions such as the van der Waals interactions between the terminal alkyl chains also contribute to the stabilization of the monolayers on the HOPG surface.[14,38] In the case of bulk crystallization, the van-der-Waals interactions between the alkyl chains and dipolar (π-stacking) interactions between the NDI cores are expected to have a dominant influence on the structure formation. We note that both these factors were absent in the case of monolayers.

The impact of the respective interactions on the size of the structural repeating units in both media can be investigated by comparing d_{LAM} with the unit cell parameter '*b*' on surface. In bulk material, d_{LAM} is always slightly larger than the corresponding $H_{37}C_{18}$-NDI-C_xH_{2x}-NDI-element which suggests interdigitated molecules in a fully stretched conformation. The unit cell parameters '*b*' on surface represents the same crystal axis of the lamellar phase in bulk. In contrast to d_{LAM}, '*b*' increases only marginally with an increasing length of the central alkyl chain. When the length of the alkyl spacer is five methylene groups or more, '*b*' becomes even smaller than the corresponding $H_{37}C_{18}$-NDI-C_xH_{2x}-NDI-element. Since a literature report on octadecyl substituted NDIs[38] and the STM images suggested that the octadecyl chains are stretched out flat, the central alkyl chains have to be partially desorbed to reduce the unit cell along the long axis which is also similar to a system reported by Schwab *et al*.[72]

■ CONCLUSIONS

A novel series of ten double NDIs was prepared and their self-assembly was explored on HOPG surfaces and in bulk. All materials (except **NDI-C4-NDI** whose solubility was too

low for an investigation) formed self-assembled monolayers on HOPG surface. All imaged monolayers had a double lamellar morphology in common which stemmed from the double NDIs being arranged in a fully stretched conformation. The investigation of the structural details of the monolayers showed that the adsorption of the terminal octadecyl chains occurred in two modes, namely in the collinear and in the non-collinear orientation. The length of the NDI connecting alkyl chain set the distance between the adsorbed NDI cores which were arranged either in the *syn*- or an *anti*-orientation. Whereas the *syn*-orientation was observed for the compounds with an alkyl spacer that was containing three or five methylene groups, an *anti*-orientation was observed for all other derivatives. The unexpected *anti*-orientation of the derivatives with an alkyl spacer containing seven, nine or eleven methylene groups was ascribed to the partial desorption of the spacer. X-Ray scattering experiments indicated the formation of lamellar lattices for all compounds in the solid state. Within the lattices, NDI cores and alkyl chains were arranged in alternating 2D sheets. When comparing the domain spacings of the crystalline bulk materials with the unit cells of the monolayers, we observed that the structural repeating units of the surface patterns were always slightly shorter than those of the bulk materials. The discrepancy of the values was relatively small for compounds with a short NDI connecting alkyl chain and increased with an increasing length of the alkyl chain. In congruence with molecular models of the imaged structures, this observation was ascribed to the partial desorption of the central alkyl chain.

Despite the fundamental differences of the interactions inducing the formation of supramolecular structures at the HOPG/1-phenyloctane interface and in bulk material, all presented double NDIs formed structurally similar lamellae in both media. However, subtle differences were identified when investigating the structural details. Whereas the partial desorption of the central alkyl chain was observed for several derivatives on surface, the formation of a second crystalline polymorph was noticed in bulk material. We found that the similarities of the structures formed in both media were decreased when the length of the central alkyl chain was increased. Such an increasing conformational freedom reduces the predictability of the formed structures and needs to be considered when designing multicomponent systems for the generation of functional interfaces.

ASSOCIATED CONTENT

Supporting Information. The supporting information is available free of charge via the Internet at http://pubs.acs.org." Synthetic procedures, supplementary ^{1}H, ^{13}C NMR, MALDI-TOF and FT-IR spectra as well as DSC traces STM images and molecular models.

AUTHOR INFORMATION

Corresponding Authors

E.W. Meijer – Laboratory of Macromolecular and Organic Chemistry, and Institute for Complex Molecular Systems, Department of Chemical Engineering and Chemistry, Eindhoven University of Technology P.O. Box 513, 5600 MB Eindhoven, The Netherlands; *orchid-org/0000*-0003-4126-7492; E-mail: *e.w.meijer@tue.nl*

Steven De Feyter – Division of Molecular Imaging and Photonics, Department of Chemistry, KU Leuven, Celestijnenlaan 200F, B 3001, Leuven, Belgium; *orchid-org/0000-0002-0909-9292;* E-mail: *steven.defeyter@kuleuven.be*

Authors

Andreas T. Rösch – Laboratory of Macromolecular and Organic Chemistry, and Institute for Complex Molecular Systems, Department of Chemical Engineering and Chemistry, Eindhoven University of Technology P.O. Box 513, 5600 MB Eindhoven, The Netherlands; *orchid-org/0000-0002-7383-903X*

Robby Reynaerts – Division of Molecular Imaging and Photonics, Department of Chemistry, KU Leuven, Celestijnenlaan 200F, B 3001, Leuven, Belgium; *orchid-org/0000-0002-2551-5145*

Brigitte A.G. Lamers – Laboratory of Macromolecular and Organic Chemistry, and Institute for Complex Molecular Systems, Department of Chemical Engineering and Chemistry, Eindhoven University of Technology P.O. Box 513, 5600 MB Eindhoven, The Netherlands

Kunal S. Mali – Division of Molecular Imaging and Photonics, Department of Chemistry, KU Leuven, Celestijnenlaan 200F, B 3001, Leuven, Belgium; *orchid-org/0000-0002-9938-6446*

Anja R.A. Palmans – Laboratory of Macromolecular and Organic Chemistry, and Institute for Complex Molecular Systems, Department of Chemical Engineering and Chemistry, Eindhoven University of Technology P.O. Box 513, 5600 MB Eindhoven, The Netherlands; *orchid-org/0000-0002-7201-1548*

Funding Sources

The authors acknowledge funding from the Dutch Ministry of Education, Culture and Science (Gravity program 024.001.035). The authors gratefully acknowledge financial support from the Fund of Scientific Research Flanders (FWO), KU Leuven - Internal Funds. This work was in part supported by FWO and FNRS under grant EOS 30489208 (2Dto3D project).

Notes

The authors declare no competing financial interest.

Author Contributions

The manuscript was written through contributions of all authors. / All authors have given approval to the final version of the manuscript. / ‡These authors contributed equally. (match statement to author names with a symbol)

Funding Sources

This work was supported financially by the Dutch Ministry of Education, Culture and Science (Gravitation Program no. 024.001.035).

ACKNOWLEDGMENT

Ralf Bovee is acknowledged for MALDI-TOF measurements. José A. Berrocal is acknowledged for fruitful discussions.

REFERENCES

(1) Goronzy, D. P.; Ebrahimi, M.; Rosei, F.; Arramel; Fang, Y.; De Feyter, S.; Tait, S. L.; Wang, C.; Beton, P. H.; Wee, A. T. S.; Weiss, P. S.; Perepichka, D. F. Supramolecular Assemblies on Surfaces: Nanopatterning, Functionality, and Reactivity. *ACS Nano* **2018**, *12*, 7445–7481.

(2) Mali, K. S.; Pearce, N.; De Feyter, S.; Champness, N. R. Frontiers of Supramolecular Chemistry at Solid Surfaces. *Chem. Soc. Rev.* **2017**, *46*, 2520–2542.

(3) Slater, A. G.; Beton, P. H.; Champness, N. R. Two-Dimensional Supramolecular Chemistry on Surfaces. *Chem. Sci.* **2011**, *2*, 1440–1448.

(4) Räisänen, M. T.; Mögele, F.; Feodorow, S.; Rieger, B.; Ziener, U.; Leskelä, M.; Repo, T. Alkyl Chain Length Defines 2D Architecture of Salophen Complexes on Liquid-Graphite Interface. *Eur. J. Inorg. Chem.* **2007**, 25, 4028–4034.

(5) Van Hove, M. A. From Surface Science to Nanotechnology. *Catal. Today* **2006**, *113*, 133–140.

(6) Elemans, J. A. A. W.; Lei, S.; De Feyter, S. Molecular and Supramolecular Networks on Surfaces: From Two-Dimensional Crystal Engineering to Reactivity. *Angew. Chem. Int. Ed.* **2009**, *48*, 7298–7333.

(7) Ringk, A.; Li, X.; Gholamrezaie, F.; Smits, E. C. P.; Neuhold, A.; Moser, A.; Van Der Marel, C.; Gelinck, G. H.; Resel, R.; De Leeuw, D. M.; Strohriegl, P. N-Type Self-Assembled Monolayer Field-Effect Transistors and Complementary Inverters. *Adv. Funct. Mater.* **2013**, *23*, 2016–2023.

(8) Smits, E. C. P.; Mathijssen, S. G. J.; Van Hal, P. A.; Setayesh, S.; Geuns, T. C. T.; Mutsaers, K. A. H. A.; Cantatore, E.; Wondergem, H. J.; Werzer, O.; Resel, R.; Kemerink, M.; Kirchmeyer, S.; Muzafarov, A. M.; Ponomarenko, S. A.; De Boer, B.; Blom, P. W. M.; De Leeuw, D. M. Bottom-up Organic Integrated Circuits. *Nature* **2008**, *455*, 956–959.

(9) Andringa, A. M.; Spijkman, M. J.; Smits, E. C. P.; Mathijssen, S. G. J.; Hal, P. A. va.; Setayesh, S.; Willard, N. P.; Borshchev, O. V.; Ponomarenko, S. A.; Blom, P. W. M.; de Leeuw, D. M. Gas Sensing with Self-Assembled Monolayer Field-Effect Transistors. *Org. Electron.* **2010**, *11*, 895–898.

(10) Casalini, S.; Bortolotti, C. A.; Leonardi, F.; Biscarini, F. Self-Assembled Monolayers in Organic Electronics. *Chem. Soc. Rev.* **2017**, *46*, 40–71.

(11) Lathrop, J. W. The Diamond Ordnance Fuze Laboratory's Photolithographic Approach to Microcircuits. *IEEE Ann. Hist. Comput.* **2013**, *35*, 48–55.

(12) Katz, H. E.; Huang, J. Thin-Film Organic Electronic Devices. *Annu. Rev. Mater. Res.* **2009**, *39*, 71–92.

(13) Pathem, B. K.; Claridge, S. A.; Zheng, Y. B.; Weiss, P. S. Molecular Switches and Motors on Surfaces. *Annu. Rev. Phys. Chem.* **2013**, *64*, 605–630.

(14) Berrocal, J. A.; Heideman, G. H.; De Waal, B. F. M.; Enache, M.; Havenith, R. W. A.; Stöhr, M.; Meijer, E. W.; Feringa, B. L. Engineering Long-Range Order in Supramolecular Assemblies on Surfaces: The Paramount Role of Internal Double Bonds in Discrete Long-Chain Naphthalenediimides. *J. Am. Chem. Soc.* **2020**, *142*, 4070–4078.

(15) Lehn, J.-M. Perspectives in Supramolecular Chemistry - From Molecular Recognition Towards Molecular Information Processing and Self-Organisation. *Angew. Chem. Int. Ed.* **1990**, *29*, 1304–1319.

(16) Dickerson, P. N.; Hibberd, A. M.; Oncel, N.; Bernasek, S. L. Hydrogen-Bonding versus van Der Waals Interactions in Self-Assembled Monolayers of Substituted Isophthalic Acids. *Langmuir* **2010**, *26*, 18155–18161.

(17) Atwood, J. L.; Barbour, L. J.; Heaven, M. W.; Raston, C. L. Controlling van Der Waals Contacts in Complexes of Fullerene C60. *Angew. Chem. Int. Ed.* **2003**, *42*, 3254–3257.

(18) McNellis, E. R.; Meyer, J.; Reuter, K. Azobenzene at Coinage Metal Surfaces: Role of Dispersive van Der Waals Interactions. *Phys. Rev. B - Condens. Matter Mater. Phys.* **2009**, *80*, 205414.

(19) Sauer, J.; Ugliengo, P.; Garrone, E.; Saunders, V. R. Theoretical Study of van Der Waals Complexes at Surface Sites in Comparison with the Experiment. *Chem. Rev.* **1994**, *94*, 2095–2160.

(20) Feringán, B.; Romero, P.; Serrano, J. L.; Folcia, C. L.; Etxebarria, J.; Ortega, J.; Termine, R.; Golemme, A.; Giménez, R.; Sierra, T. H-Bonded Donor-Acceptor Units Segregated in Coaxial Columnar Assemblies: Toward High Mobility Ambipolar Organic Semiconductors. *J. Am. Chem. Soc.* **2016**, *138*, 12511–12518.

(21) Barth, J. V.; Weckesser, J.; Cai, C.; Günter, P.; Bürgi, L.; Jeandupeux, O.; Kern, K. Building Supramolecular Nanostructures at Surfaces by Hydrogen Bonding. *Angew. Chem. Int. Ed.* **2000**, *39*, 1230–1234.

(22) Slater, A. G.; Perdigão, L. M. A.; Beton, P. H.; Champness, N. R. Surface-Based Supramolecular Chemistry Using Hydrogen Bonds. *Acc. Chem. Res.* **2014**, *47*, 3417–3427.

(23) Zhou, H.; Dang, H.; Yi, J. H.; Nanci, A.; Rochefort, A.; Wuest, J. D. Frustrated 2D Molecular Crystallization. *J. Am. Chem. Soc.* **2007**, *129*, 13774–13775.

(24) Griessl, S.; Lackinger, M.; Edelwirth, M.; Hietschold, M.; Heckl, W. M. Self-Assembled Two-Dimensional Molecular Host-Guest Architectures from Trimesic Acid. *Single Mol.* **2002**, *3*, 25–31.

(25) Esch, J. Van; Feyter, S. De; Kellogg, R. M.; Schryver, F. De; Feringa, B. L. Self-Assembly of Bisurea Compounds in Organic Solvents and on Solid Substrates. *Chem. Eur. J.* **1997**, 3, 1238-1243.

(26) De Feyter, S.; Grim, P. C. M.; Van Esch, J.; Kellogg, R. M.; Feringa, B. L.; De Schryver, F. C. Nontrivial Differentiation between Two Identical Functionalities within the Same Molecule Studied by STM. *J. Phys. Chem. B* **1998**, *102*, 8981–8987.

(27) Gutzler, R.; Fu, C.; Dadvand, A.; Hua, Y.; MacLeod, J. M.; Rosei, F.; Perepichka, D. F. Halogen Bonds in 2D Supramolecular Self-Assembly of Organic Semiconductors. *Nanoscale* **2012**, *4*, 5965–5971.

(28) Yoon, J. K.; Son, W. J.; Chung, K. H.; Kim, H.; Han, S.; Kahng, S. J. Visualizing Halogen Bonds in Planar Supramolecular Systems. *J. Phys. Chem. C* **2011**, *115*, 2297–2301.

(29) Vijayaraghavan, S.; Ecija, D.; Auwärter, W.; Joshi, S.; Seufert, K.; Drach, M.; Nieckarz, D.; Szabelski, P.; Aurisicchio, C.; Bonifazi, D.; Barth, J. V. Supramolecular Assembly of Interfacial Nanoporous Networks with Simultaneous Expression of Metal-Organic and Organic-Bonding Motifs. *Chem. Eur. J.* **2013**, *19*, 14143–14150.

(30) De Ruiter, G.; Lahav, M.; Van Der Boom, M. E. Pyridine Coordination Chemistry for Molecular Assemblies on Surfaces. *Acc. Chem. Res.* **2014**, *47*, 3407–3416.

(31) Stepanow, S.; Lingenfelder, M.; Dmitriev, A.; Spillmann, H.; Delvigne, E.; Lin, N.; Deng, X.; Cai, C.; Barth, J. V.; Kern, K. Steering Molecular Organization and Host-Guest Interactions Using Two-Dimensional Nanoporous Coordination Systems. *Nat. Mater.* **2004**, *3*, 229–233.

(32) Ilan, B.; Florio, G. M.; Hybertsen, M. S.; Berne, B. J.; Flynn, G. W. Scanning Tunneling Microscopy Images of Alkane Derivatives on Graphite: Role of Electronic Effects. *Nano Lett.* **2008**, *8*, 3160–3165.

(33) Lee, S. L.; Chi, C. Y. J.; Huang, M. J.; Chen, C. H.; Li, C. W.; Pati, K.; Liu, R. S. Shear-Induced Long-Range Uniaxial Assembly of Polyaromatic Monolayers at Molecular Resolution. *J. Am. Chem. Soc.* **2008**, *130*, 10454–10455.

(34) Binnig, G.; Quate, C. F. Atomic Force Microscope. *Phys. Rev. Lett.* **1986**, *56*, 930–933.

(35) Topple, J. M.; Burke, S. A.; Fostner, S.; Grütter, P. Thin Film Evolution: Dewetting Dynamics of a Bimodal Molecular System. *Phys. Rev. B - Condens. Matter Mater. Phys.* **2009**, *79*, 205414.

(36) Binnig, G.; Rohrer, H. Scanning Tunneling Microscopy. *IBM J. Res. Dev.* **1986**, *30*, 355–369.

(37) Sweetman, A. M.; Jarvis, S. P.; Sang, H.; Lekkas, I.; Rahe, P.; Wang, Y.; Wang, J.; Champness, N. R.; Kantorovich, L.; Moriarty, P. Mapping the Force Field of a Hydrogen-Bonded Assembly. *Nat. Commun.* **2014**, *5*, 3931.

(38) Miyake, Y.; Nagata, T.; Tanaka, H.; Yamazaki, M.; Ohta, M.; Kokawa, R.; Ogawa, T. Entropy-Controlled 2D Supramolecular Structures of N,N'-Bis(n-Alkyl)- Naphthalenediimides on a HOPG Surface. *ACS Nano* **2012**, *6*, 3876–3887.

(39) Chen, T.; Chen, Q.; Pan, G. B.; Wan, L. J.; Zhou, Q. L.; Zhang, R. Ben. Linear Dislocation Tunes Chirality: STM Study of Chiral Transition and Amplification in a Molecular Assembly on an HOPG Surface. *Chem. Commun.* **2009**, 2649–2651.

(40) Berrocal, J. A. J. A.; Teyssandier, J.; Goor, O. J. G. M. G. M.; De Feyter, S.; Meijer, E. W.; Feyter, S. De; Meijer, E. W.

Supramolecular Loop Stitches of Discrete Block Molecules on Graphite: Tunable Hydrophobicity by Naphthalenediimide End-Capped Oligodimethylsiloxane. *Chem. Mater.* **2018**, *30*, 3372–3378.

(41) Tao, F.; Bernasek, S. L. Understanding Odd-Even Effects in Organic Self-Assembled Monolayers. *Chem. Rev.* **2007**, *107*, 1408–1453.

(42) Fang, H.; Giancarlo, L. C.; Flynn, G. W. Packing of Br(CH2)10COOH and Br(CH2)11COOH on Graphite: An Odd-Even Length Effect Observed by Scanning Tunneling Microscopy. *J. Phys. Chem. B* **1998**, *102*, 7421–7424.

(43) Stals, P. J. M.; Smulders, M. M. J.; Martín-Rapún, R.; Palmans, A. R. A.; Meijer, E. W. Asymmetrically Substituted Benzene-1,3,5-Tricarboxamides: Self-Assembly and Odd-Even Effects in the Solid State and in Dilute Solution. *Chem. Eur. J.* **2009**, *15*, 2071–2080.

(44) Zhang, H.; Yin, Q.; Liu, Z.; Gong, J.; Bao, Y.; Zhang, M.; Hao, H.; Hou, B.; Xie, C. An Odd-Even Effect on Solubility of Dicarboxylic Acids in Organic Solvents. *J. Chem. Thermodyn.* **2014**, *77*, 91–97.

(45) Blumstein, A.; Thomas, O. Odd-Even Effect in Thermotropic Liquid Crystalline 4,4′-Dihydroxy-2,2′-Dimethylazoxybenzene-Alkanedioic Acid Polymers. *Macromolecules* **1982**, *15*, 1264–1267.

(46) Yang, S.; Xu, X.; Zhu, Y.; Niu, R.; Xu, C.; Peng, Y.; Cheng, X.; Jia, X.; Xu, X.; Lu, J.; Ye, Y. Odd-Even Layer-Number Effect and Layer-Dependent Magnetic Phase Diagrams in MnBi2Te4. *Phys. Rev. X* **2021**, *11*, 011003.

(47) Amara, F. Ben; Dionne, E. R.; Kassir, S.; Pellerin, C.; Badia, A. Molecular Origin of the Odd − Even Effect of Macroscopic Properties of n - Alkanethiolate Self-Assembled Monolayers: Bulk or Interface? *J. Am. Chem. Soc.* **2020**, *142,* 13051-13061.

(48) Yang, K.; Cai, Z.; Jaiswal, A.; Tyagi, M.; Moore, J. S.; Zhang, Y. Dynamic Odd–Even Effect in Liquid n-Alkanes near Their Melting Points. *Angew. Chem. Int. Ed.* **2016**, *55*, 14090–14095.

(49) Boiling points and structures of hydrocarbons http://chemistry.elmhurst.edu/vchembook/501hcboilingpts.html.

(50) Thalladi, V. R.; Boese, R.; Weiss, H. C. The Melting Point Alternation in α,ω-Alkanedithiols. *J. Am. Chem. Soc.* **2000**, *122*, 1186–1190.

(51) Kim, K.; Plass, K. E.; Matzger, A. J. Structure of and Competitive Adsorption in Alkyl Dicarbamate Two-Dimensional Crystals. *J. Am. Chem. Soc.* **2005**, *127*, 4879–4887.

(52) Alba, M. D.; Castro, M. A.; Clarke, S.; Medina, S.; Messe, L.; Millán, C.; Orta, M. M.; Perdigón, A. C. Preferential Adsorption from Binary Mixtures on Graphite: The n-Decane-n-Heptan-1-ol System. *J. Phys. Chem. C* **2009**, *113*, 3176–3180.

(53) Wang, X.; Lee, S. Y.; Miller, K.; Welbourn, R.; Stocker, I.; Clarke, S.; Casford, M.; Gutfreund, P.; Skoda, M. W. A. Cation Bridging Studied by Specular Neutron Reflection. *Langmuir* **2013**, *29*, 5520–5527.

(54) Laker, Z. P. L.; Marsden, A. J.; De Luca, O.; Pia, A. Della; Perdigão, L. M. A.; Costantini, G.; Wilson, N. R. Monolayer-to-Thin-Film Transition in Supramolecular Assemblies: The Role of Topological Protection. *Nanoscale* **2017**, *9*, 11959–11968.

(55) Castro, M. A.; Clarke, S. M.; Inaba, A.; Dong, C. C.; Thomas, R. K. Crystalline Monolayer of Dodecanoic Acid Adsorbed on Graphite from N-Heptane Solution. *J. Phys. Chem. B* **1998**, *102*, 777–781.

(56) Herwig, K. W.; Matthies, B.; Taub, H. Solvent Effects on the Monolayer Structure of Long N-Alkane Molecules Adsorbed on Graphite. *Phys. Rev. Lett.* **1995**, *75*, 3154–3157.

(57) Labat, S.; Guichet, C.; Thomas, O.; Gilles, B.; Marty, A. Microstructural Analysis of AU/NI Multilayers Interfaces by SAXS and STM. *Appl. Surf. Sci.* **2002**, *188*, 182–187.

(58) Jiao, X.; Maniam, S.; Langford, S. J.; McNeill, C. R. Influence of Side-Chain Length and Geometry on the Thermal Expansion Behavior and Polymorphism of Naphthalene Diimide-Based Thin Films. *Phys. Rev. Mater.* **2019**, *3*, 013606.

(59) Fu, C.; Lin, H. P.; Macleod, J. M.; Krayev, A.; Rosei, F.; Perepichka, D. F. Unravelling the Self-Assembly of Hydrogen Bonded NDI Semiconductors in 2D and 3D. *Chem. Mater.* **2016**, *28*, 951–961.

(60) Kaneda, Y.; Stawasz, M. E.; Sampson, D. L.; Parkinson, B. A. STM Investigations of the Two-Dimensional Ordering of Perylenetetracarboxylic Acid N-Alkyl-Diimides on HOPG and MoS2 Surfaces. *Langmuir* **2001**, *17,* 6185–6195.

(61) Hak, J.; Sabin-Lucian, S.; Lee, W. Y.; Könemann, M.; Höffken, H. W.; Röger, C.; Schmidt, R.; Chung, Y.; Chen, W. C.; Würthner, F.; Bao, Z. High-Performance Air-Stable n-Type Organic Transistors Based on Core-Chlorinated Naphthalene Tetracarboxylic Diimides. *Adv. Funct. Mater.* **2010**, *20*, 2148–2156.

(62) Kobaisi, M. Al; Bhosale, S. V. S. V.; Latham, K.; Raynor, A. M.; Bhosale, S. V. S. V. Functional Naphthalene Diimides: Synthesis, Properties, and Applications. *Chem. Rev.* **2016**, *116*, 11685–11796.

(63) Bell, T. D. M.; Bhosale, S. V.; Forsyth, C. M.; Hayne, D.; Ghiggino, K. P.; Hutchison, J. A.; Jani, C. H.; Langford, S. J.; Lee, M. A. P.; Woodward, C. P. Melt-Induced Fluorescent Signature in a Simple Naphthalenediimide. *Chem. Commun.* **2010**, *46*, 4881–4883.

(64) Milita, S.; Liscio, F.; Cowen, L.; Cavallini, M.; Drain, B. A.; Degousée, T.; Luong, S.; Fenwick, O.; Guagliardi, A.; Schroeder, B. C.; Masciocchi, N. Polymorphism in: N, N ′-Dialkyl-Naphthalene Diimides. *J. Mater. Chem. C* **2020**, *8*, 3097–3112.

(65) Berrocal, J. A.; Zha, R. H.; De Waal, B. F. M.; Lugger, J. A. M.; Lutz, M.; Meijer, E. W. Unraveling the Driving Forces in the Self-Assembly of Monodisperse Naphthalenediimide-Oligodimethylsiloxane Block Molecules. *ACS Nano* **2017**, *11*, 3733–3741.

(66) Dey, A.; Kalita, A.; Iyer, P. K. High-Performance n-Channel Organic Thin-Film Transistor Based on Naphthalene Diimide. *ACS Appl. Mater. Interfaces* **2014**, *6*, 12295–12301.

(67) Kakinuma, T.; Kojima, H.; Ashizawa, M.; Matsumoto, H.; Mori, T. Correlation of Mobility and Molecular Packing in Organic Transistors Based on Cycloalkyl Naphthalene Diimides. *J. Mater. Chem. C* **2013**, *1,* 5395–5401.

(68) Ma, Z.; Geng, H.; Wang, D.; Shuai, Z. Influence of Alkyl Side-Chain Length on the Carrier Mobility in Organic Semiconductors: Herringbone: Vs. Pi-Pi Stacking. *J. Mater. Chem. C* **2016**, *4*, 4546–4555.

(69) Jones, B. A.; Facchetti, A.; Wasielewski, M. R.; Marks, T. J. Tuning Orbital Energetics in Arylene Diimide Semiconductors. Materials Design for Ambient Stability of n-Type Charge Transport. *J. Am. Chem. Soc.* **2007**, *129*, 15259–15278.

(70) Baumgartner, B.; Svirkova, A.; Bintinger, J.; Hametner, C.; Marchetti-Deschmann, M.; Unterlass, M. M. Green and Highly Efficient Synthesis of Perylene and Naphthalene Bisimides in Nothing but Water. *Chem. Commun.* **2017**, *53*, 1229–1232.

(71) Tambara, K.; Ponnuswamy, N.; Hennrich, G.; Pantoş, G. D. Microwave-Assisted Synthesis of Naphthalenemonoimides and N-Desymmetrized Naphthalenediimides. *J. Org. Chem.* **2011**, *76*, 3338–3347.

(72) Schwab, M. G.; Takase, M.; Mavrinsky, A.; Pisula, W.; Feng, X.; Gámez, J. A.; Thiel, W.; Mali, K. S.; De Feyter, S.; Müllen, K. Torands Revisited: Metal Sequestration and Self-Assembly of Cyclo-2,9-Tris-1,10-Phenanthroline Hexaaza Macrocycles. *Chem. Eur. J.* **2015**, *21*, 8426–8434.

(73) Chesterfield, R. J.; McKeen, J. C.; Newman, C. R.; Ewbank, P. C.; Da Silva Filho, D. A.; Brédas, J. L.; Miller, L. L.; Mann, K. R.; Frisbie, C. D. Organic Thin Film Transistors Based on N-Alkyl Perylene Diimides: Charge Transport Kinetics as a Function of Gate Voltage and Temperature. *J. Phys. Chem. B* **2004**, *108*, 19281–19292.

(74) Ichikawa, M.; Yokota, Y.; Jeon, H. G.; Banoukepa, G. D. R.; Hirata, N.; Oguma, N. Comparative Study of Soluble Naphthalene Diimide Derivatives Bearing Long Alkyl Chains as N-Type Organic Thin-Film Transistor Materials. *Org. Electron.* **2013**, *14*, 516–522.

(75) Van Genabeek, B.; De Waal, B. F. M.; Palmans, A. R. A.; Meijer, E. W. Discrete Oligodimethylsiloxane-Oligomethylene Di- and Triblock Co-Oligomers: Synthesis, Self-Assembly and Molecular Organisation. *Polym. Chem.* **2018**, *9*, 2746–2758.

(76) Park, J.; Lee, S. H.; Choi, M. Y.; Moon, C. J.; Kim, T. H. Crystal Structure of N, N ′-Bis[3-(Methylsulfanyl)Propyl]-1,8:4,5-

Naphthalenetetracarboxylic Diimide. *Acta Crystallogr. Sect. E Crystallogr. Commun.* **2019**, *75*, 934–938.
(77) Groszec, A. J. Selective Adsorption at Graphite/Hydrocarbon Interfaces. *Proc. R. Soc. A* **1970**, *314*, 473-498.

(maximum width for single-column artwork, 3.3 in. (8.5 cm); maximum width for double-column artwork, 7 in. (17.8 cm)). **NOTE**: If you are submitting a Table of Contents graphic, please insert the graphic at the end of the file.

SYNOPSIS TOC (Word Style "SN_Synopsis_TOC"). If you are submitting your paper to a journal that requires a synopsis graphic and/or synopsis paragraph, see the Instructions for Authors on the journal's homepage for a description of what needs to be provided and for the size requirements of the artwork.

To format double-column figures, schemes, charts, and tables, use the following instructions:

Place the insertion point where you want to change the number of columns
From the **Insert** menu, choose **Break**
Under **Sections**, choose **Continuous**
Make sure the insertion point is in the new section. From the **Format** menu, choose **Columns**
In the **Number of Columns** box, type **1**
Choose the **OK** button

Now your page is set up so that figures, schemes, charts, and tables can span two columns. These must appear at the top of the page. Be sure to add another section break after the table and change it back to two columns with a spacing of 0.33 in.

Table 1. Example of a Double-Column Table

Column 1	Column 2	Column 3	Column 4	Column 5	Column 6	Column 7	Column 8

Authors are required to submit a graphic entry for the Table of Contents (TOC) that, in conjunction with the manuscript title, should give the reader a representative idea of one of the following: A key structure, reaction, equation, concept, or theorem, etc., that is discussed in the manuscript. Consult the journal's Instructions for Authors for TOC graphic specifications.

Insert Table of Contents artwork here